2008 IEEE International Conference on
Robotics and Automation
Pasadena, CA, USA, May 19-23, 2008

An Untethered Magnetically Actuated Micro-Robot Capable of Motion on Arbitrary Surfaces

Steven Floyd, Chytra Pawashe, and Metin Sitti

Abstract— **This work presents an untethered magnetic micro-robot with dimensions of 250 μm x 130 μm x 100 μm. The robot is composed entirely of neodymium-iron-boron fabricated using laser micro-machining. It is actuated by a system of five macro-scale electromagnets. By using electromagnets to control the robot, the surface on which the robot operates need not be specialized, smooth, patterned, nor conductive. Two control methods, both based on periodic excitation of the robot, are attempted and compared. Controllable motion at speeds in excess of 2.8 mm/s, approximately 11 body lengths per second, is demonstrated. Teleoperated motion in two dimensions is shown, and the assembly of micro-particles is demonstrated underwater. Potential future applications include micro-scale manipulation, fabrication, and assembly of micro-systems.**

I. Introduction

Though many miniature robots exist on the centimeter scale, true micron-scale robots, with all characteristic lengths on the order of 10 to 100 μm, are still quite rare. The fundamental challenge with decreasing robot size below the millimeter scale is providing power and actuation to the robot [1]. Most current micro-robots today rely on external actuation and/or power to function, and usually have further limitations as well.

Micro-robots conventionally require specialized surfaces or environments in which to function. For some, surfaces must be smooth, regular, and flat, like a silicon wafer [2]. They use piezoelectric elements to achieve stick-slip motion. Defects or aberrations in the surface can cause a step to fail, or cause an actuation element to become stuck, adversely affecting the robot's motion.

Some micro-robots require a patterned surface to actuate or provide power to the micro-robot. Electrical power can be provided to the robot through conductive surfaces that alternate between different voltage levels at different points in space [3]. Alternatively, actuation of robots that are electrostatically coupled to a substrate can be achieved with surfaces covered in a non-conductive layer [4]. These scratch-drive micro-robots receive both actuation and control instructions through the patterned surface, and cannot operate without it.

Other micro-robots require attached tethers [5], [6]. These 'walking chips' have micro-actuators, and can carry many times their body weight, but are large–often several millimeters on a side. There are also micro-robots that can only function in a fluid medium. For some, viscous drag is balanced against a magnetic force [7], [8] or the magnetic field is used to actuate a component [9]. For others, bacteria are used as a propulsive mechanism, which can only move themselves while immersed in a compatible fluid [10].

There exists few robots with all dimensions on the micron scale [4], [7], [10], and each is subject to one or more of the aforementioned restrictions. The micro-robot presented in this paper has fewer limitations on surfaces where it can function. Actuated by large-scale electromagnets, it does not require any physical tethers to move. Controlled by algorithms that dynamically adjust the magnetic field, it does not require a patterned work surface or electrostatic coupling to a sub-surface. Its only limitations are that the work surface cannot be composed of a ferromagnetic or strongly diamagnetic material, nor can the surface itself be magnetized, and the robot must remain within the working volume of the electromagnets.

Micro-robots that do not rely on specialized surfaces for power delivery and control are a vital step toward advancing the field of micro-robotics, which is filled with many potential applications. Examples include micro-manipulation of micro-components, and micro-assembly and fabrication of hybrid micro-systems. Tetherless micro-robots with appropriate tools can be used for micro-scale measurement and surface inspection. More advanced micro-robots could even be used for undetectable surveillance as micro unmanned vehicles, or as micro-surgeons in medical applications inside living bodies.

II. Experimental Setup

Five independent electromagnetic coils were constructed large enough to contain a cube 10 cm on a side, which contains the working volume. Of these coils, four were placed upright to control the direction and gradient of the horizontal magnetic field, and one is placed below the work plane to control the electromagnetic clamping, shown in Fig. 1. Within the tolerances of machining, the coils were constructed to be identical, with the same dimensions, wire gauge, and number of turns of the wire. Parameters for each of the electromagnets are provided in Table I. Within a cube approximately 2 cm on a side, fringing fields are less than 5% of the total magnetic field [11]. Imaging of the the magnetic micro-robot is accomplished with a CCD camera (WV-CD 110A, Panasonic Inc.) connected to a variable magnification microscope lens. For high-framerate video, a

S. Floyd is with the Department of Mechanical Engineering, Carnegie Mellon University, Pittsburgh, PA 15213, USA srfloyd@andrew.cmu.edu

C. Pawashe is with the Department of Mechanical Engineering, Carnegie Mellon University, Pittsburgh, PA 15213, USA csp@andrew.cmu.edu

M. Sitti is with the Department of Mechanical Engineering, Carnegie Mellon University, Pittsburgh, PA 15213, USA sitti@cmu.edu

978-1-4244-1647-9/08/$25.00 ©2008 IEEE.

high speed camera (Phantom V7.0, Vision Research Inc.) and an additional microscope lens was placed horizontally inside one of the four upright magnets to achieve a side view of the micro-robot during actuation. Control of the electromagnetic coils is performed by a PC with a data acquisition system (6032E and AT-AO-10, National Instruments Inc.) at a control bandwidth of 1 kHz. The coils are powered by custom electronic amplifiers, controlled by the PC. To measure the magnetic fields, linear hall-effect sensors are used (A1321, Allegro Microsystems Inc.).

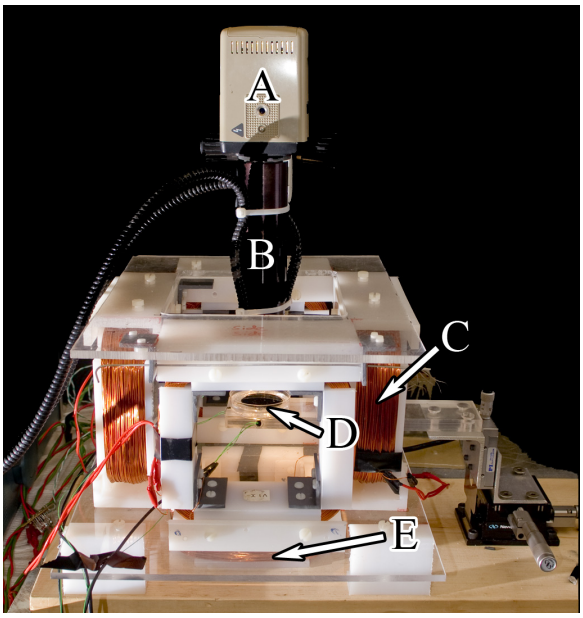

Fig. 1. Photograph of the electromagnetic coil setup, where (A) is the camera, (B) is the microscope lens, (C) is one of four horizontal coils that move the micro-robot within the plane, (D) is the wafer where the micro-robot resides, and (E) is the clamping coil beneath the wafer that holds the micro-robot to the surface.

Description	Value	Units
Inner length	0.120	m
Outer length	0.157	m
Number of Turns (N_T)	510	–
Effective Length ($2a$)	0.1385	m
Coil Resistance	10.0	Ω
Distance From Center	.099	m
Maximum Field at Center (c)	6.5	mT
Maximum Gradient at Center	149	mT/m

TABLE I
ELECTROMAGNET PROPERTIES

III. MAGNETIC FORCE MODELING

The micro-robot used in this work is derived from neodymium-iron-boron (NdFeB), a hard magnetic material, which allows the micro-robot to retain its magnetization in the absence of a magnetic field. To determine the magnitude of the forces and the feasibility of robot motion, a computer model of the system was created.

A. Magnetic Field

For square turn electromagnets, the Helmholtz spacing is 0.5445 times the length of a side [11]. To maintain Helmholtz spacing, coil pairs would have to be "nested" inside each other, and would require different wrapping or drive currents to produce similar magnetic fields. While Helmholtz spacing would be preferred for the generation of uniform magnetic fields [11], this ability was sacrificed so that the electromagnets in all directions could be built to the same size, as seen in Fig. 1. Orthogonal pairs are used to decouple forces in the x and y-directions.

Inside of the control volume, the principle of superposition is valid for determining the magnetic field at a point in space. Hence, the contributions from all five electromagnets can be determined and then added together. To determine the contribution of each electromagnet, one must apply the Biot-Savart law for each square turn coil:

$$\vec{B}(\vec{X}) = \frac{\mu_0 N_T I}{4\pi} \oint_S \frac{\vec{dl'} \times \vec{a}_R}{R^2} \tag{1}$$

where $\vec{B}(\vec{X})$ is the magnetic field at the robot's position $\vec{X} = x\vec{e}_x + y\vec{e}_y + z\vec{e}_z$, μ_0 is the permeability of free space ($4\pi \times 10^{-7}$), N_T is the number of turns in the coil, I is the current flowing through the coil, $\vec{dl'}$ is an infinitesimal line segment along the direction of integration, $\vec{a}_R$ is the unit vector from the line segment to a point in space of interest, and R is the distance from the line segment to the space of interest.

For a square turn coil, this contour integral simplifies into four line integrals, the definite integral of which exists and can be evaluated at the end points [12]. For the x-directed coils, the primary and fringe magnetic fields at any point in space can be determined by evaluating the following:

$$R = \sqrt{(x-c)^2 + (y-y_j)^2 + (z-z_i)^2} \tag{2}$$

$$B_x = \frac{\mu_0 N_T I}{4\pi} \sum_{i=1}^{2} \sum_{j=1}^{2} (-1)^{i+j} * \frac{(z-z_i)(y-y_j)}{R} * \left[\frac{1}{(x-c)^2+(y-y_j)^2} + \frac{1}{(x-c)^2+(z-z_i)^2} \right] \tag{3}$$

$$B_y = \frac{\mu_0 N_T I}{4\pi} \sum_{i=1}^{2} \sum_{j=1}^{2} (-1)^{i+j+1} * \left(\frac{(z-z_i)(x-c)}{R} * \left[\frac{1}{(x-c)^2+(y-y_j)^2} \right] \right) \tag{4}$$

$$B_z = \frac{\mu_0 N_T I}{4\pi} \sum_{i=1}^{2} \sum_{j=1}^{2} (-1)^{i+j+1} * \left(\frac{(x-c)(y-y_j)}{R} * \left[\frac{1}{(x-c)^2+(z-z_i)^2} \right] \right) \tag{5}$$

$$z = [a, -a], y = [a, -a] \tag{6}$$

where B_i is the magnetic field in the i direction, a is half the effective length of the magnet, and c is $\pm$ the distance from the center, where the $\pm$ is evaluated based upon the location of the coil of interest (i.e. plus for the coil in the positive x or positive y-directions). Similar equations are used for the y-directed and clamping coils.

This derivation is for a concentrated electromagnet, i.e. all the current carrying wires can be described by a single line with zero thickness. This assumption is valid because the playing field is small in comparison to the magnetic coils, and the distribution of wires within each electromagnet is small compared to the size of the magnet. As a result, an effective length must be used instead of the actual inner or outer length; these values are listed in Table I.

B. Magnetic Forces

Within a magnetic field any magnetized object, in this case the micro-robot, will experience both a torque and a force. This magnetic torque is proportional to the magnetic field strength, and acts in a direction to bring the internal magnetization of the object into alignment with the field. The magnetic force is proportional to the gradient of the magnetic field, and acts to move the object to a local maximum. The equations that govern these interactions are:

$$\vec{T_m} = V_m \vec{M} \times \vec{B}(\vec{X}) \tag{7}$$

$$\vec{F_m} = V_m (\vec{M} \bullet \nabla) \vec{B}(\vec{X}) \tag{8}$$

where $\vec{T_m}$ is the torque the robot experiences, V_m is the volume of the robot, and $\vec{M}$ is the magnetization of the robot (assumed to be uniform) [7], [13].

To find the gradient in the magnetic field, a numerical derivative method is utilized:

$$\frac{\partial B_x(x,y,z)}{\partial x} \approx \frac{B_x(x+\delta,y,z) - B_x(x-\delta,y,z)}{2\delta} \tag{9}$$

where $\delta = L/10$. This method is similarly applied to each component of the magnetic field in each direction to determine the theoretical forces on the robot. To determine the applied torque, the magnetic field is evaluated at the center of the robot's body. It was found that the maximum force and torque that can be exerted on the micro-robot are 240 nN and 10.5 $\mu N \cdot mm$, respectively.

C. Magnetic Micro-Robot

In modeling the micro-robot, we assume that the micro-robot is a rectilinear solid, with constant, uniform properties such as density and magnetization. These properties are presented in Table II.

Description	Value	Units
Length (L)	250	μm
Width (W)	130	μm
Height (H)	100	μm
Density (ρ)	7880	kg/m^3
Mass (m)	25.6	ng
Weight (mg)	251	nN
Magnetization (M)	5×10^5	A/m

TABLE II
MAGNETIC ROBOT PROPERTIES

From experimental observation, the micro-robot appears to exhibit a stick-slip motion when actuated by a pulsed magnetic field (see Fig. 3). To model the dynamics of the magnetic micro-robot, we restrict modeling to the side-view of the micro-robot, in the $x-z$ plane, shown in Fig. 2. The robot is modeled with its center of mass (COM) at $\vec{X}$, an orientation angle θ from the ground, with a distance r from its COM to a corner, and an angle ϕ determined from geometry. The robot experiences external forces, including its weight mg, a normal force N, an adhesive force to the surface F_{adh}, an x-directed externally applied magnetic force F_x, a z-directed externally applied magnetic force F_z, an externally applied magnetic torque T_y, a rotational damping torque D_y, and a Coloumb sliding friction force F_f. F_f depends on N, the sliding friction coefficient μ, and the velocity of the contact point, $\frac{dP_x}{dt}$, where (P_x, P_z) is the point of contact between the robot and the surface.

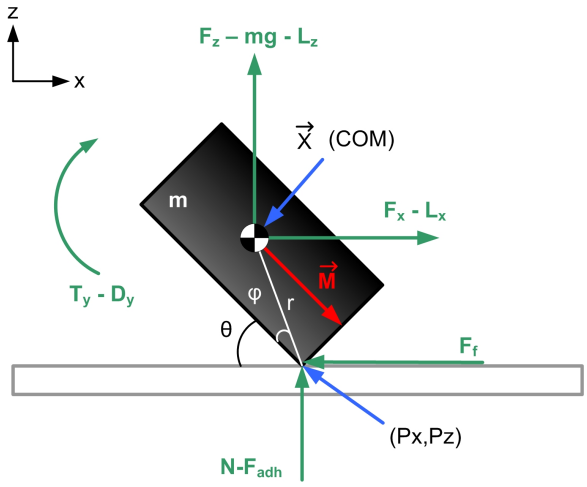

Fig. 2. Schematic of the rectangular magnetic micro-robot with applied external forces. Magnetization vector is denoted by $\vec{M}$.

The equations of motion are formed and numerically solved using Gauss-Seidel iteration. A Runge-Kutta solver is employed to numerically solve the time-varying motion of the micro-robot, where the inputs of the simulation are the voltages on the electromagnetic coils. In Fig. 3, the results of the simulation are displayed in comparison to experimental results, where similar stick-slip behavior is observed in both cases. The detailed dynamic modeling of this stick-slip behavior will be presented in another publication.

IV. ROBOT FABRICATION

To create the robot, a magnetized piece of NdFeB was cut using a laser machining system (LaserMill, New Wave Research Inc.). First, the NdFeB was cut parallel to the direction of magnetization, making planar slices approximately 100 μm thick. These slices were then laid flat so that the magnetization of the slice was in a horizontal plane. Robots were then cut from these slices such that the magnetization vector was pointing towards the front of the robot.

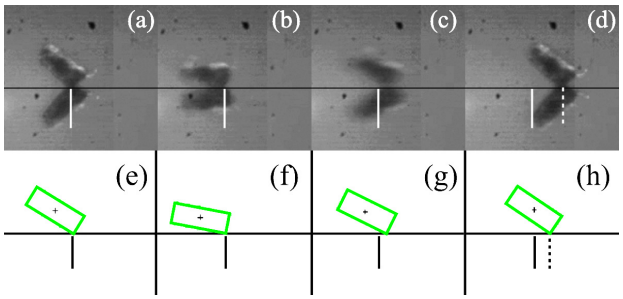

Fig. 3. Stick-slip motion of the micro-robot observed with a high speed camera, compared to simulated results from a side-view. (a) The robot is initially at its steady state angle, and the point of contact is highlighted by a solid white line. (b) When the magnetic field changes, the robot rocks downward, changing its angle relative to the silicon wafer. (c) During the next upswing, the robot slides forward. The former contact point is highlighted with a solid white line. (d) After slipping forward, the robot assumes its steady state angle again at a new position, shown by a dashed white line. Analogous steps are performed in simulation in images (e) through (h).

High translational speeds, small laser spot size, and low cutting depths per pass were employed to minimize local demagnetization due to heating by the laser. A scanning electron micrograph of a sample robot is shown in Fig. 4. Other versions of the robot are 'H' shaped instead of 'V' shaped so that motion in either direction is more symmetric.

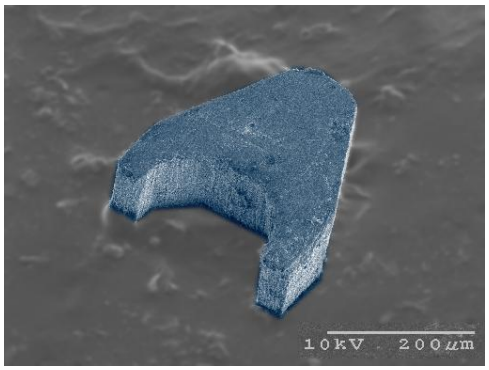

Fig. 4. A false-color scanning electron micrograph of a sample permanent magnet micro-robot. The opening is toward the front of the robot and is present for future studies of micro-scale object manipulation.

V. Control Signals

Two different control methods were employed to actuate the micro-robot. Both use short duration, periodic fluctuations in the magnetic field to keep the micro-robot's velocity reasonable. In this way, the micro-robot is made to take small, controlled steps.

A. In Plane Pulsing

In the first control method, called In Plane Pulsing (IPP), the in-plane magnetic field is pulsed at varying frequencies. Initially the clamping coil and an in-plane coil magnetic fields are established to orient the micro-robot and secure it to the surface. This magnetic field is chosen large enough such that the robot turns and orients, but not translate. By increasing the magnetic field gradient periodically using a sawtooth waveform, stick-slip motion is induced in the robot, moving it in small steps. The magnetic fields produced for motion in one direction using IPP are shown in Fig. 5, where the x-directed magnetic field represents the in-plane magnetic field, and the z-directed field corresponds to the clamping field.

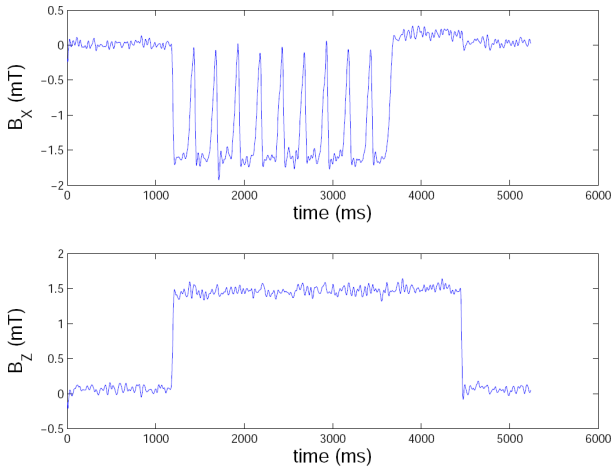

Fig. 5. Plots of the magnetic fields in the x and z-direction produced during linear translation with IPP control. Hall-effect sensors placed inside the working volume are used to record magnetic fields during experiment.

B. Out of Plane Pulsing

A second control method using Out of Plane Pulsing (OPP) is demonstrated. Instead of the in-plane electromagnet being pulsed as in IPP control, the clamping electromagnet is pulsed with a sawtooth waveform in OPP. This pulsing also induces stick-slip behavior in the micro-robot, causing it to translate. The magnetic fields produced for motion in one direction using OPP is shown in Fig. 6.

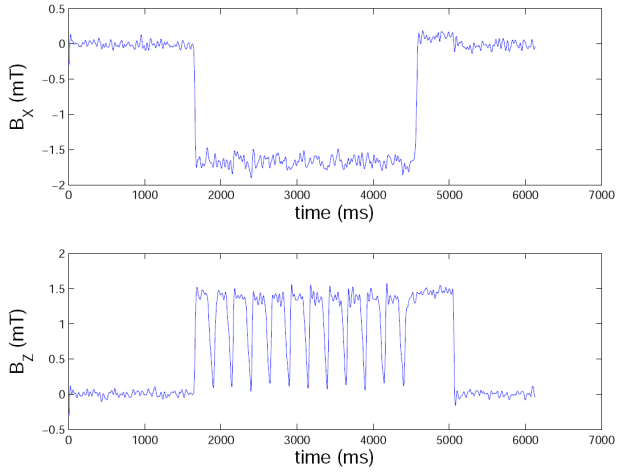

Fig. 6. Plots of the magnetic fields in the x and z-direction produced during linear translation with OPP control.

VI. Experimental Results

All testing was performed on the back side of a 4-inch silicon wafer in open, untreated air. No special polishing or

preparation was performed on the wafer. For both control methods, testing was done at various frequencies at a constant maximum coil voltage of 30 V, which corresponds to a maximum magnetic field of 2.9 mT near the center, and also at various maximum coil voltages with a constant pulse frequency of 30 Hz. During each test, video was recorded of the micro-robot translating across the field of view.

After each experiment, the video was analyzed to determine the robot's steady state velocity. The first several frames after the robot initiated motion were discarded to remove the effect of any transient behavior. Two frames, one near the beginning and one near the end of the robot's journey, were chosen. In each, the robot's central position was determined and the total travel distance was measured in pixels. The total time for travel was also recorded to determine the velocity. A conversion ratio to map the image to experimental coordinates in microns/pixel was empirically determined. All tests were performed with the robot moving from the left, $x-$, coil toward the right, $x+$, coil. Any drift perpendicular to the direction of travel was ignored; only motion in the desired direction was used to determine velocity.

Robot velocity as a function of frequency for both IPP and OPP control seems to be linear at low frequencies, and then saturates at higher frequencies, seen in Figs. 7 and 8. For both sets of data, maximum coil voltage was kept at 30 V. OPP control, with the oscillations in the clamping coil, has much higher linear velocities, exceeding 2.8 mm/s with a 70 Hz drive signal. By comparison, the maximum velocity under IPP control was only 700 μm/s.

For IPP control, there appears to be a linear relationship between maximum coil voltage and velocity, shown in Fig. 9. Alternatively, Fig. 10 shows that there is no clear dependence of velocity on the maximum coil voltage for OPP control at a constant frequency of 30 Hz, remaining relatively constant over the entire range.

Global positioning of the robot was possible by using a succession of motions in the x and y-directions on the working surface. A trace of robot position over time, controlled

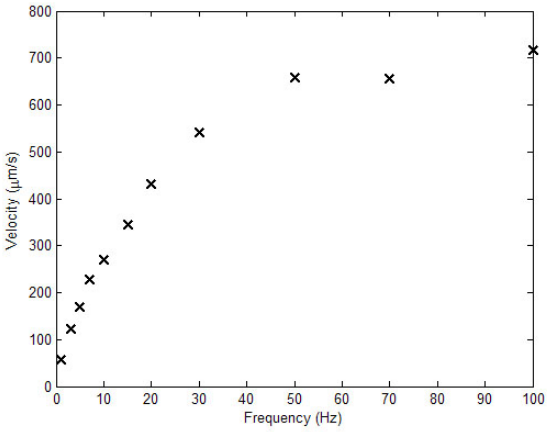

Fig. 7. Experimental robot velocity at varying frequencies using IPP, with a constant maximum coil voltage of 30 V.

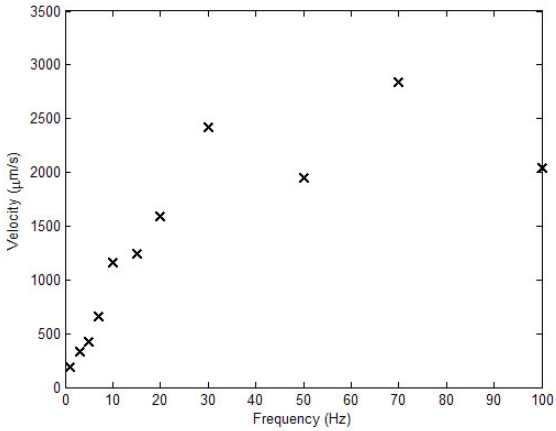

Fig. 8. Experimental robot velocity at varying frequencies using OPP, with a constant maximum coil voltage of 30 V.

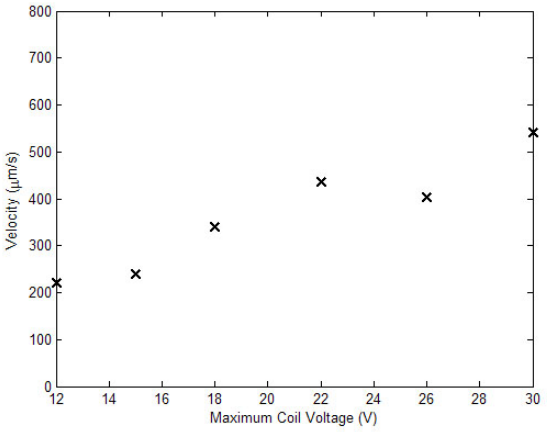

Fig. 9. Experimental robot velocity at varying coil voltages using IPP, with a constant pulse frequency of 30 Hz.

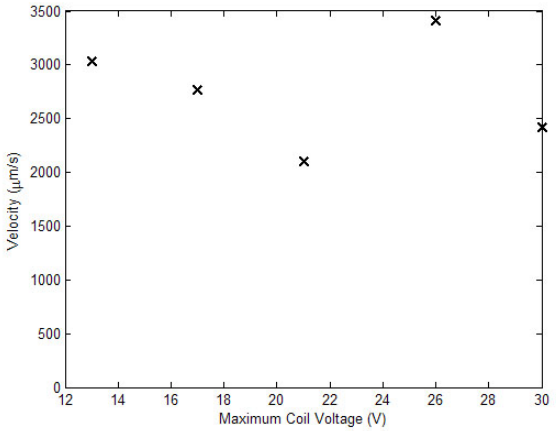

Fig. 10. Experimental robot velocity at varying coil voltages using OPP, with a constant pulse frequency of 30 Hz.

via teleoperation, is shown in Fig. 11. The robot spins in place while turning, so the turning radius is essentially zero. As an application, the manipulation of 116 μm polystyrene beads is demonstrated, shown in Fig. 12. In this experiment the micro-robot is used to push the beads, and is teleoperated on a silicon wafer under a droplet of water, which reduces undesirable stiction effects when manipulating the beads. Videos of these experiments are available at [14].

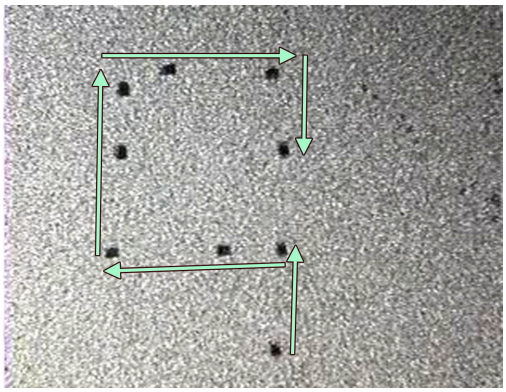

Fig. 11. Top view of a micro-robot's path as viewed under a microscope using teleoperated control. Several frames from a movie are superimposed with the path taken by the robot between frames is shown with arrows.

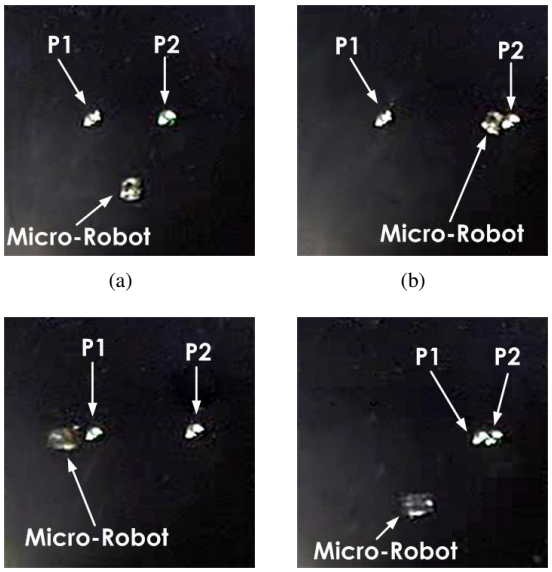

Fig. 12. Teleoperated manipulation of two 116 μm polystyrene beads underwater using a magnetic micro-robot. In (a) the initial configuration is shown, in (b) particle 2 (P2) is pushed and positioned, in (c) particle 1 (P1) is pushed, and the final assembly is shown in (d).

VII. Discussion and Conclusion

The asymptotic behavior of robot velocity at higher frequencies may be due to hardware limitations. The output waveforms, when discretized at 1 kHz, may not be continuous enough to properly actuate the micro-robot. Much like an impact drive device, if the waveform is too symmetric, the robot will simply vibrate in place instead of moving linearly.

While the linear dependence of robot velocity to the maximum coil voltage is anticipated, seen for IPP in Fig. 9, the unclear dependence shown for OPP in Fig. 10 was unexpected.

It can easily be seen that OPP control is more conducive for attaining higher linear velocities. Consequently, the robot must have larger average step sizes than with IPP control. As a control possibility, OPP can be used for coarse robot motion and IPP can be used for fine adjustment in a particular micro-manipulation task.

As a function of frequency, the robot velocity saturates above 60 Hz for both IPP and OPP control. A linear relationship between maximum coil voltage and robot velocity exists for IPP control, but no clear relationship exists for OPP control. Higher velocities are achieved using OPP control, with a maximum velocity greater than 2.8 mm/s, or 11 robot body lengths per second.

Future work will include adapting the system for both coarse and fine motion control. Vision algorithms are being developed for closed loop high-level control of the micro-robot. Applications in micro-object manipulation are also being explored.

References

[1] M. Sitti, "Microscale and nanoscale robotics systems - Characteristics, state of the art, and grand challenges," IEEE Robotics and Automation Magazine, vol. 14, no. 1, pp. 53-60, March 2007.

[2] S. Martel et. al., "Three-Legged Wireless Miniature Robots for Mass-Scale Operations at the Sub-Atomic Scale," Proceedings of the 2001 IEEE International Conference on Robotics and Automation, Seoul, Korea, pp. 3423- 3428, 2001.

[3] S. Martel, "Special surface for power delivery to wireless micro-electro-mechanical systems," J. Micromech Microeng., 15, pp. S251-258, 2005.

[4] B. R. Donald, C. G. Levey, C. D. McGray, I. Paprotny, and D. Rus, "An Untethered, Electrostatic, Globally Controllable MEMS Micro-Robot," J. MEMS, Vol. 15, no. 1, pp. 1-15, 2006.

[5] T. Ebefors, J. U. Mattsson, E. Kalvesten, and G. Stemme, "A Walking Silicon Micro-Robot," The 10th Int Conference on Solid-State Sensors and Actuators (Transducers99), Sendai, Japan, pp 1202-1205. 1999.

[6] P. E. Kladitis, and V. M. Bright, "Prototype Microrobots for Micro-positioning and Micro-unmanned Vehicles," Sensors and Actuators, Vol. 80, No. 2, pp. 132-137, 2000.

[7] K. Yesin, K. Vollmers, and B. Nelson, "Modeling and Control of Untethered Biomicrorobots in a Fluidic Environment Using Electro-magnetic Fields," The International Journal of Robotics Research, Vol. 25, No. 5-6, pp. 527-536, 2006.

[8] A. Yamazaki et. al., "Wireless micro swimming machine with magnetic thin film," Journal of Magnetism and Magnetic Materials, Vol. 272-276, pp. E1741-E1742, 2004.

[9] R. Dreyfus et. al., "Microscopic artificial swimmers," Nature, Vol. 437, pp. 862-865, 2005.

[10] B. Bekham and M. Sitti, "Bacterial flagella-based propulsion and on/off motion control of microscale objects," Applied Physics Letters, Vol. 90, pp. 2390223904, 2007.

[11] W. Frix, G. Karady, and B. Venetz, "Comparison of Calibration Systems for Magnetic Field Measurement Equipment," IEEE Transactions on Power Delivery, Vol. 9, pp. 100-108, 1994.

[12] D. K. Cheng, *Field and Wave Electromagnetics*, 2nd ed. New York: Addison-Wesley Publishing Co., 1992.

[13] T. Boyer, "The Force on a Magnetic Dipole," Am. J. Phys., Vol. 56, Issue 8, pp. 688-692, 1987.

[14] Magnetically Actuated Micro-Robots, NanoRobotics Laboratory, http://nanolab.me.cmu.edu/projects/MagneticMicroRobot/